LASER WELDING DISSIMILAR REFLECTIVE ALLOYS

M.H. McCay, S. Gopinathan, F. Kahlen, L. Speigel
The University of Tennessee Space Institute (UTSI)
Center for Laser Applications
Tullahoma, TN 37388-8897

Overview

This project, jointly sponsored by Rocketdyne and CSTAR, involves the development of laser joining of materials which have heretofore been impractical to bond. Of particular interest are joints between stainless steel and copper and also aluminum 6061 to aluminum 2219. CSTAR has a unique opportunity in this area since both the process and development and diagnostics are of interest to industry. Initial results using the pulse tailored laser welding technique developed in CLA for joining crack sensitive materials have proven promising for the aluminum joints based upon metallurgical and electronic microprobe analysis. Declaration of success requires additional mechanical testing. A CW technique has been applied to the stainless-copper joining with some preliminary success. These joints are of significant interest for aeronautics and rocket propulsion applications and the project is expected to continue.

The following describes the work accomplished during 1993 on the Laser Welding of Dissimilar Alloy project for each task defined in the Statement of Work.

TASK 1: LASER PROCESSING DATA BASE:

The aim of this database system is to provide information on (i) The properties of the materials to be joined and (ii) The weldability of the material using different types of lasers as well as other conventional/nonconventional joining methods. The emphasis is on laser welding of materials. This menu-driven, user-friendly database will also provide prominent references for further in-depth information. Programming on this database is essentially completed and data entry has been done on basic material properties for 280 aluminum and copper alloys.

TASK 2: ALTERNATE LASERS AND WELDING TECHNIQUES:

(a) Al2219/Al6061 Joining:

(i) Nd:YAG Laser Welding of Al2219 to Al6061

Low power pulsed Nd:YAG laser welding was performed at CSTAR on a Lumonics, JK701 laser capable of 150 Watts average power. Samples of Al6061 and Al2219 were butt welded using Argon as the cover gas. Al4047 shims were used as filler material. The welds were characterized by insufficient penetration and root porosity.

(ii) Multiwave Laser Welding of Al2219 to Al6061

High power continuous wave Nd:YAG laser butt welding was done at Lumonics in Livonia, MI at 2000 Watts using various cover gases. It was observed that the use of He, Ar and N_2 resulted in inconsistent coupling and incomplete penetration. Samples welded using compressed air however exhibited better coupling.

(iii) Copper Vapor Laser Welding of Al2219 to Al6061

Samples were sent to Rocketdyne to provide to Lawrence Livermore Labs for processing.

(iv) Electron Beam Welding of Al2219 to Al6061

Samples were processed at AEDC.

(v) TIG Welding of Al2219 to Al6061

Typical TIG welds between the two alloys were provided and evaluation showed that there does not appear to be very much mixing.

(b) Copper-Stainless Steel Joining:

(i) Electron Beam Welding

Electron beam butt welding of copper-stainless steel was carried out at AEDC using the following conditions: 100kv, 15MA, 22 1/2"/Min, X amplitude 1%, Y amplitude 1%, 100 hZ frequency and gun to work distance of 10.00. Two samples were processed on-seam, one sample was processed 1 mm on the copper side and one sample was processed 1 mm on the steel side. The samples exhibited complete penetration. Preliminary microstructural evaluation revealed cracking and insufficient mixing of the steel and copper. The

1 M.H. McCay, Professor ESM, UTSI
2 S. Gopinathan, UTSI
3 F. Kahlen, UTSI
4 L. Speigel, Technical Monitor, Rocketdyne

electron beam was also observed to "wander" towards the stainless steel side during welding.

TASK 3: PROCESS PARAMETER DEVELOPMENT AND OPTIMIZATION

(a) CO_2 Laser Welding of Al2219 to Al6061:

Bead-on-plate laser welding was carried out using both continuous-wave as well as pulsed CO_2 laser welding in order to study the effect these techniques have on laser coupling with the aluminum alloys. For the same average delivered laser power, enhanced coupling resulted in weld widths an order of magnitude higher for pulsed laser welding compared to cw welding. A comparison between the top bead widths produced by pulsed and cw welding with the same average power revealed that the weld widths are an order of magnitude higher in the pulsed welds. This is probably attributable to the leading edge spike which occurs on each pulse.

Having established the effectiveness of pulse tailoring, autogenous butt welds were made between Al2219 and Al6061 plates using a matrix of pulsing conditions and cover gases. The pulse-on time was kept constant and the pulse duty cycle and hence the input power were varied by changing the pulse-off time.

In order to characterize the Al2219-Al6061 butt welds, the top and bottom beads of the butt welds were photographed and weld bead width measurements made. The butt welds were later cross-sectioned, mounted, polished, etched and metallographically evaluated.

The effect of cover gas and pulse duty cycle on weld widths was also evaluated. It is observed that in general, the top bead widths increased with increase in pulse duty cycle for all assist gases. The welds made with argon as the assist gas were the widest, while helium resulted in the narrowest welds. Nitrogen and compressed air welds exhibited widths that were in between those of helium and argon. Pulse duty cycle seemed to have a bigger effect on weld penetration depth than cover gas. Full penetration was achieved in all samples for a duty cycle above 44% i.e. (20ms/25ms on/off times).

(b) CO_2 welding of Copper to Stainless Steel:

For the case of copper to stainless steel, continuous wave was determined to be the preferred mode. Autogenous butt laser welding experiments on copper-stainless steel samples were carried out using helium, nitrogen, compressed air and argon as the shield gases. Figure 1 shows a weld cross-section made with compressed air as the cover gas. The cross section accentuates the problem of porosity encountered by the use of compressed air. The same problem is apparent in Figure 2, which shows the cross-section of a weld made with ambient air as the cover gas. The weld made with inert argon as the cover gas showed both porosity as well as fusion zone cracking. The cross-section of the butt weld made using He revealed only slight porosity and no cracking was observed. The welds made with compressed air and ambient air were fully penetrated while those made with helium and argon showed incomplete penetration. The position of the laser beam with respect to the interface between the two materials was very critical to successful welding.

Another experiment was carried out in order to study the importance of beam position on the weld integrity. The position was varied in 0.1mm increments from the copper side to the stainless steel side. When the 3000 Watt continuous wave laser beam was made to impinge on the copper side of the assembly at distances of 0.1 to 0.5mm from the interface, there was no coupling of laser beam energy and no resultant weld. When the beam impinged on the steel side up to 0.3mm from the interface, coupling and penetration resulted. It was noted that in this case, the two pieces were physically joined, but the joint was very fragile and could easily be broken. At further distances there was no effect. A copper-steel joint was also produced by the laser beam impinging the assembly at the interface. A visual inspection of the joint revealed visible mixing between the constituents of the two materials.

TASK 4: PROCESS MONITORING AND BEAM DIAGNOSTICS:

The spectroscopic measurements of the composition of the near-surface plasma induced during laser processing can provide significant information on the welding parameters. To obtain this information, an experimental technique of spectral measurements using an Optical Multichannel Analyzer (OMA) was designed for CO_2 laser welding.

Two types of spectral measurements were carried out:

1. Spatially and temporally unresolved measurements were made of plasma plume composition during the welding of SS304, Al2219, Al6061, Cu, and SS304. The spectral investigations of the plasma plume were also carried out for the dissimilar metals laser welding. The plasma plume image was created on the OMA entrance slot using a lens. The axis of plasma plume image coincided with the OMA slot, and the detected data represent the spectra integrated over the plasma plume length. The spectra near the surface plasma were measured for the cases of welding Al6061 to Al2219 and stainless steel SS304 to copper. The spectra were

detected in spectral regions from 380 nm to 520 nm and from 580 nm to 720nm. These data show that the spectrum for the case of welding of different aluminum alloys is the combination of spectra for the welding of separate alloys. For example, the line of CrI occurs only in spectra of Al6061 and not in the spectra of Al2219 since only Al6061 contains the element Cr. This line can be observed for the welding of Al6061 to Al2219.

Stainless steel 304 contains copper, thus, it was expected that the spectra of welding of SS304 to copper would differ only by the relative intensity of the copper line, unlike the case of welding different alloys containing different elements. The spectral data proves this expectation. The relative intensity of the copper line 579 nm is higher for the case of steel to copper welding. Figure 3 shows the relative intensity of the CuI to the MnI as a function of the beam location with respect to the joint between the copper and 304 stainless steel.

2. Measurements of plasma composition without temporal resolution and with spatial resolution along the laser beam/plasma plume axis were made during the welding of SS304 and Al2219 in the spectral region 570-710nm.

The results from the first set of measurements showed that it is possible to detect the different species in the plasma/vapor plume and consequently it may be possible to monitor the weld parameters by measuring the spectral composition of the plume.

The results from the second set of measurements showed that a detectable boundary exists between the vapor plasma and the surrounding gas plasma. It means that by measuring the temporal dynamics of the boundary location one can detect instabilities in the welding process, since the boundary location depends strongly on the vapor pressure, which in turn depends on the weld temperature and molten metal hydrodynamics (keyhole dynamics). This boundary measurement technique could prove to be a very sensitive on-line diagnostic tool to monitor weld quality.

(ii) High Speed Video Photography:
High speed photography of the welding process was carried out using a Kodak EktaPro high speed camera capable of filming 1000 frames/sec. Since the pulsing rates were on the millisecond scale, the framing speed was ideal to study the welding process. In Figure 4, a digitized image of the recording of the welding process is illustrated.

TASK 5: SAMPLE EVALUATION AND TESTING:
(a) Al2219/Al6061 Joining:
The microstructure of the welded samples was metallographically analyzed. The observations have been summarized in Table I. At low duty cycles (40%) the samples were not fully penetrated and cracking was observed for all samples. At higher duty cycles (20/15,20/20), the welds made with argon as the shield gas exhibited low porosity and no cracking. The welds using helium as the cover gas showed some degree of cracking in all pulsing conditions. The aluminum butt welds using compressed air as the cover gas exhibited extensive porosity. The nitrogen welds exhibited no cracking but did show some porosity. The welds fusion zone is also characterized by the presence of certain inclusions. Similar inclusions have been observed during the laser welding of Al1100 under a nitrogen atmosphere. They were identified as aluminum nitride, AlN. Similar lamellar inclusions were also reported in studies of the feasibility of nitrating of aluminum using TIG welding with argon-nitrogen mixed shield gas.

Electron microprobe analysis and elemental X-ray mapping of the weld zone were performed in order to determine the distribution of the alloying elements. A typical SEM micrograph of the Al2219 weld zone and the corresponding silicon image are illustrated in Figures 5(a) and (b) respectively. The unaffected Al2219 region consists of elongated solid solution grains with second phase particles of $CuAl_2$ and $(Fe,Mn)_3SiAl_{12}$. This region is followed by the Al2219/Al6061 fusion zone which exhibits a columnar dendritic structure bounded by a region consisting of equalized grains. The silicon map on the Al2219 side shows the presence of silicon in the weld zone. Figure 6(a) show the Al6061 weld zone interface. The Al6061 base structure reveals Mg_2Si particles in the aluminum solid solution grains adjacent to the fusion region. Figure 6(b) shows the corresponding X-ray map of copper in the Al6061 side of the fusion zone. The presence of copper on this side of the fusion zone is apparent. From the X-ray maps in Figures 5(b) and 6(b) the good mixing of the major constituents is apparent.

Hardness measurements were made along the weld cross-section. It is observed that there is a modest drop in hardness along the center of the weld, the minimum hardness being 83VPN.

(b) Copper-Stainless Steel Welding:
Initial microstructural evaluation indicated that the best microstructures were obtained by using He and compressed air as the assist gases. Electron Microprobe analysis was carried out on the He welds to study mixing

of the various alloying elements of the steel with copper. As shown in Figure 7(a), the steel/weld interface shows three regions. The base steel structure on the left is followed by the first fusion zone, referred to here as the "steel fusion zone". The steel fusion zone is characterized by a iron-copper matrix with a dispersion of particles. The EDS spectrum of these particles (Figure 7(b)) reveals that they are copper rich. The steel fusion zone is followed by the regular fusion zone which consists of circular regions (later determined to be iron-rich regions) dispersed in a copper-steel mixture. X-Ray maps for copper, iron, nickel and chromium corresponding to Figure 7(a) were also generated. Equilibrium thermodynamics dictates that the solid solubility of Cu in Fe is very small and that of Ni in Cu is very high. The Xray maps however revealed much better than expected mixing between copper and iron. The copper rich regions in the steel fusion zone were found to contain nickel as well. This could be due to a Cu-Ni solid solution formation in this region. The vigorous stirring in the melt combined with the high temperatures encountered during laser processing may be responsible. Figure 8 shows the weld-copper interface. Large elongated copper grains are present in the heat affected zone surrounding the fusion zone. The X-ray maps for iron, copper, nickel and chromium revealed the degree of mixing between the constituents of the two material. It was apparent that the copper and steel constituents have indeed mixed. Figure 9(a) shows the copper steel fusion zone. The fusion zone consists of iron-rich regions in the matrix of the copper-steel fusion zone. Figure 9(b) represents the EDS spectrum of the iron-rich region. The X-ray traces for iron and copper in the weld fusion zone revealed the presence of some sort of copper-iron solid solution matrix with some iron rich regions in between.

AMENDED STATEMENT OF WORK

TASK 1: CO_2 Processing of Narloy Z

A set of trial experiments was performed to identify pertinent CO_2 laser operating conditions which affect the laser melting of 2 mm thick Narloy Z samples. The matrix is given in Table II for three of the samples. Laser power was kept constant (approximately 3 kW delivered to sample), and traverse speed, beam focal position, and surface finish were modified. An argon flood cover gas was used during all experiments.

A total of four 2.5 cm x 5 cm samples have been processed: Six processing runs were performed on the first sample. The surface of the first sample was unmodified for the first five runs except for cleaning with methanol. For the sixth run, powdered graphite was applied to enhance the surface energy absorption.

One half of the second sample was dipped in a graphite/methanol mixture and allowed to dry so that the surface was coated with carbon. This was done to enhance the absorption of the CO_2 laser energy. One calibration run (run number one) was performed on the unmodified (except for methanol cleaning) half and four runs (runs four through five) were made on the coated half.

The surface of sample three was modified by oxidizing the surface. The third sample was placed in a furnace at 500C for approximately 10 minutes to form an oxide layer. Ten runs were performed on sample three.

Sample four was treated the same as sample three so that an oxide film was present on the sample surface. It was instrumented with thermocouples so that high sample rate (100hz) temperature measurements could be made during processing. Five runs were made on sample four. Two thermocouples were placed on the sample using a high conductivity, high temperature cement. The thermocouples were sampled at an acquisition rate of 100hz using a multi-channel, high-speed amplifier system and a pc-based A/D data acquisition board. One of the thermocouples was apparently destroyed by the plasma generated during the first processing run, therefore only one thermocouple was measured during runs 2-5. It also appears that some melting of the thermocouple shield wire occurred during the last two runs (runs 4 and 5) so that the data for these runs is questionable. Thus, it is believed that only run 1,2, and 3 have valid measurements.

Figure 10 shows cross-sections of three of the Narloy Z single glazes made with the CO_2 laser. Particles of zirconium are present in the base alloy but are no longer visible in the glazed material. The glazed region also appears to have solidified with a cellular dendritic structure. SEM and Energy Dispersive Spectroscopy (EDS) analysis however, does indicate the presence of zirconium distributed throughout the glazed region. Figure 11 presents the relationship between the traverse speed and the width of the glaze track for the different surfaces and focal locations.

Spectral investigations of the plasma plume were made during CO_2 glazing with argon and helium as the cover gases. The zirconium spectra were not visible when using argon due to the high background intensity. Spectra taken with helium as the cover gas revealed the presence of zirconium along with copper and silver.

TASK 2: Nd:YAG Processing of Narloy Z

A set of trial experiments were performed on 3 mm thick Narloy samples with two surface finishes unmodified and sanded. Both surfaces were cleaned with methanol before processing. A 5mm x 25mm matrix was done at each condition using an argon cover gas. Four sets of glazing was done on each surface at the conditions given in Table III.

Figure 12 shows surface view of glazed tracks processed the Nd:YAG laser. Additional samples have been sent to Lumonics for processing with the Multiwave Nd:YAG.

FUTURE WORK

1. Narloy Z processing:

Results indicate that it is feasible to glaze Narloy Z using either a CO_2 or a Nd:YAG laser. The glazed regions exhibit cellular/dendritic solidification structure and according to energy dispersive spectroscopy, contain dissolved zirconium. Since it is not known if the dissolved zirconium can impart the desired creep properties to the glazed region, these regions should be further characterized. In addition, since there is zirconium present in the laser sustained plasma which is formed during processing, further analysis should be done to determine the extent to which zirconium is lost as a result of this mechanism.

The Nd:YAG laser offers the greatest flexibility for glazing Narloy Z since the beam can be delivered fiber-optically. Further glazing studies should be conducted using the 2kW multiwave Nd:YAG.

The joining of reflective materials such as copper and Narloy Z to themselves is a great interest to industry. The narrow fusion zone provided by the laser offers great promise for this task. It is suggested that further effort be expended to determine the laser joining parameters and analyze the resultant structure in copper and Narloy Z joints.

2. Dissimilar metal joining:

The copper/stainless steel and Al2219/Al6061 joints produced using the laser appear to be sound and have constituent mixing. Mechanical and chemical tests should be conducted on these and joints of other selected dissimilar materials to substantiate that the joints have desirable properties.

3. Development of spectral weld monitor:

Based on spectral analysis taken during the joining of copper to 304 stainless steel, it is possible to use the relative peak heights of elements in the alloys to determine the beam location with respect to the joint. This knowledge is extremely significant when welding dissimilar materials (whether it be by electron beam or laser) since any variation in beam location will significantly alter the mixing and therefore the soundness of the joint. A simple detector/feedback control device could be built that would be applicable to lasers or electron beams and provide the necessary control to maintain the beam in the correct position during welding.

Table I: Summary of the low magnification evaluation of the Al2219/Al6061 weld cross-sections.

	Duty Cycle %			
Cover Gas	40%	44%	50%	57%
Argon	C,NP	P,C	P	P
Compressed Air	C,NP	C,P,PO	P,PO	P,PO
Nitrogen	C,P,I, NP	P,PO,I	P,PO,I	P,I
Helium	C,PO, NP	P,C	P,C	P,C

Table II
CO_2 Glazing Parameters

Sample	Run	Surface	Focus	Speed
I	1	As received	O	25.0
	2	As received	0	12.5
	3	As received	+2	12.5
	4	As received	+1	12.5
	5	As received	+1	19.0
	6	As received	+1	19.0
II	1	As received	+1	19.0
	2	Graphite Paste	+1	25.0
	3	Graphite Paste	+1	19.0
	4	Graphite Paste	+2	19.0
	5	Graphite Paste	+1	35.0
III	1	Oxidized	+1	35.0
	2	Oxidized	+1	50.0
	3	Oxidized	+2	50.0
	4	Oxidized	+2	35.0
	5	Oxidized	+2	25.0
	6	Oxidized	+2	12.5
	7	Oxidized	-2	6.0
	8	Oxidized	-2	25.0
	9	Oxidized	-4	25.0
	10	Oxidized	-3	25.0

TASK 3: Microstructural Evaluation

Table III
Nd:YAG Glazing Parameters

Sample#	Surface	Power (Watts)	Energy/pulse	Step Distance	Rep Rate
1	Unmodified	18	0.62	100	30
2	Unmodified	27	0.91	100	30
3	Unmodified	42	1.42	100	30
4	Unmodified	56	1.90	100	30
5	Sanded	18	0.61	100	30
6	Sanded	27	0.93	100	30
7	Sanded	42	1.42	100	30
8	Sanded	56	1.89	100	30

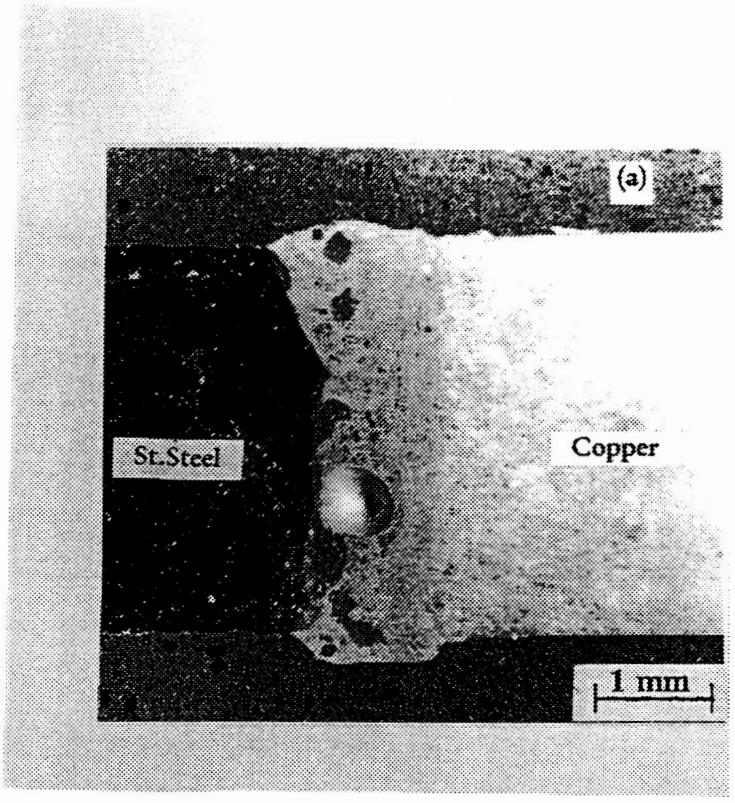

Figure 1 - Cross-section of copper/stainless steel weld. Compressed air cover gas.

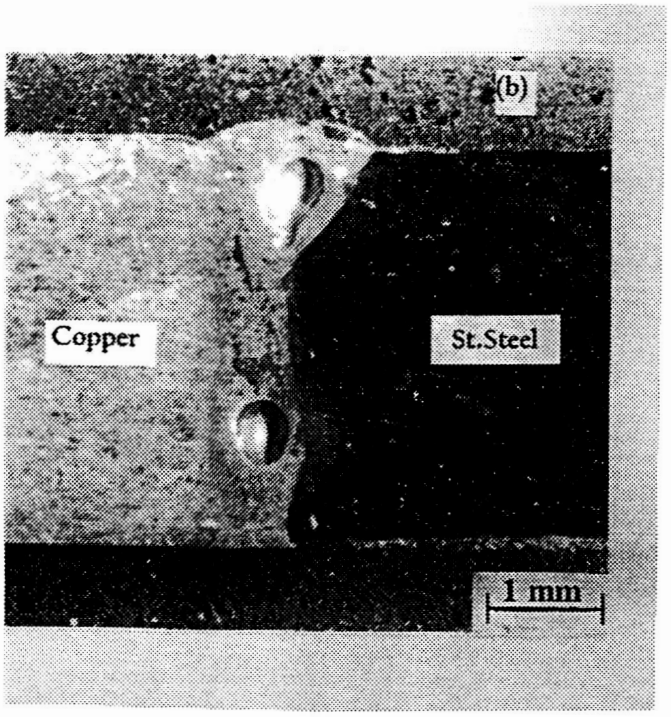

Figure 2 - Cross-section of copper/stainless steel weld. Ambient air cover gas.

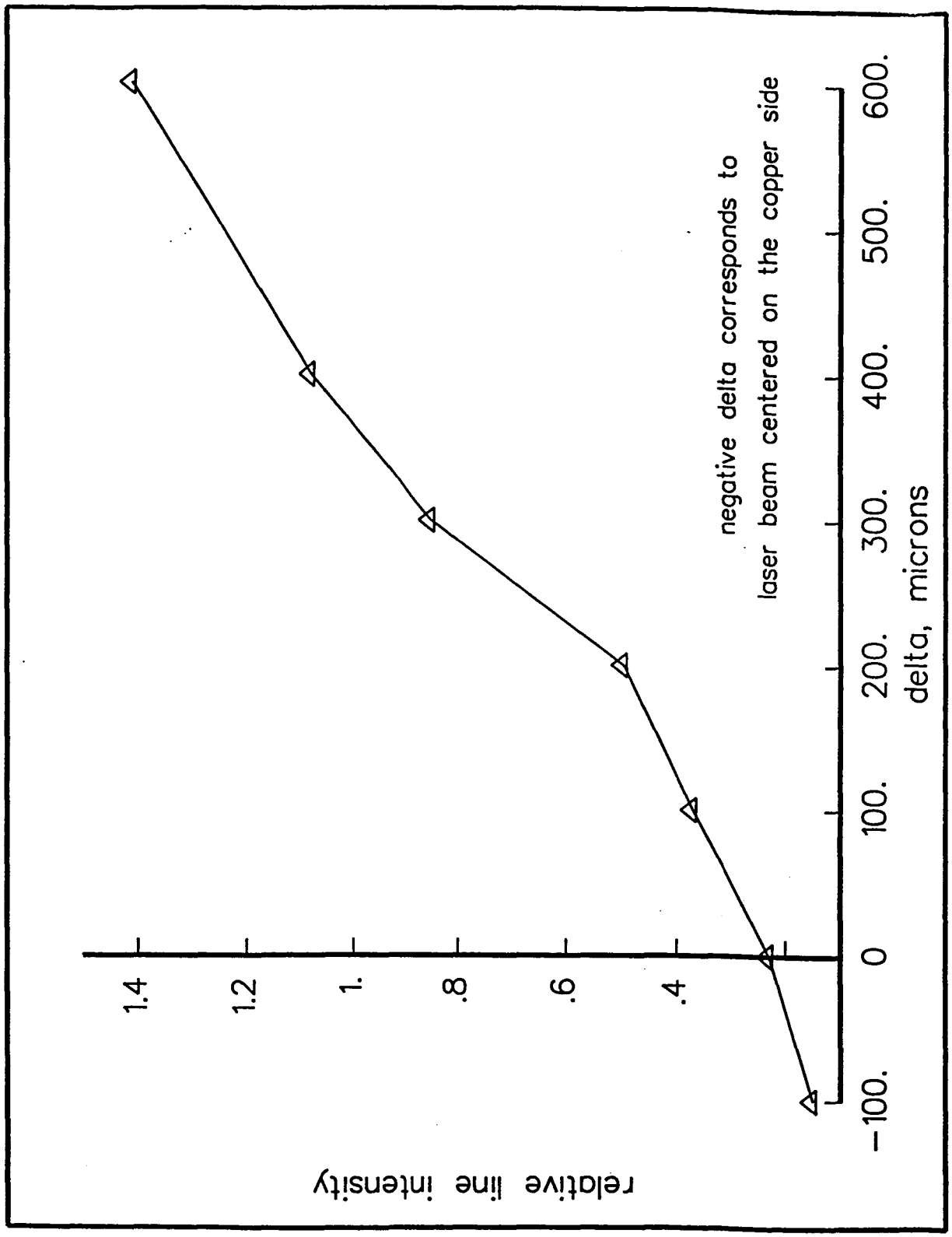

Figure 3 - Relative intensity of CuI line to MnI line as a function of laser beam location with respect to the joint.

Figure 4 - High speed photograph of the laser welding of Al2219 to Al6061.

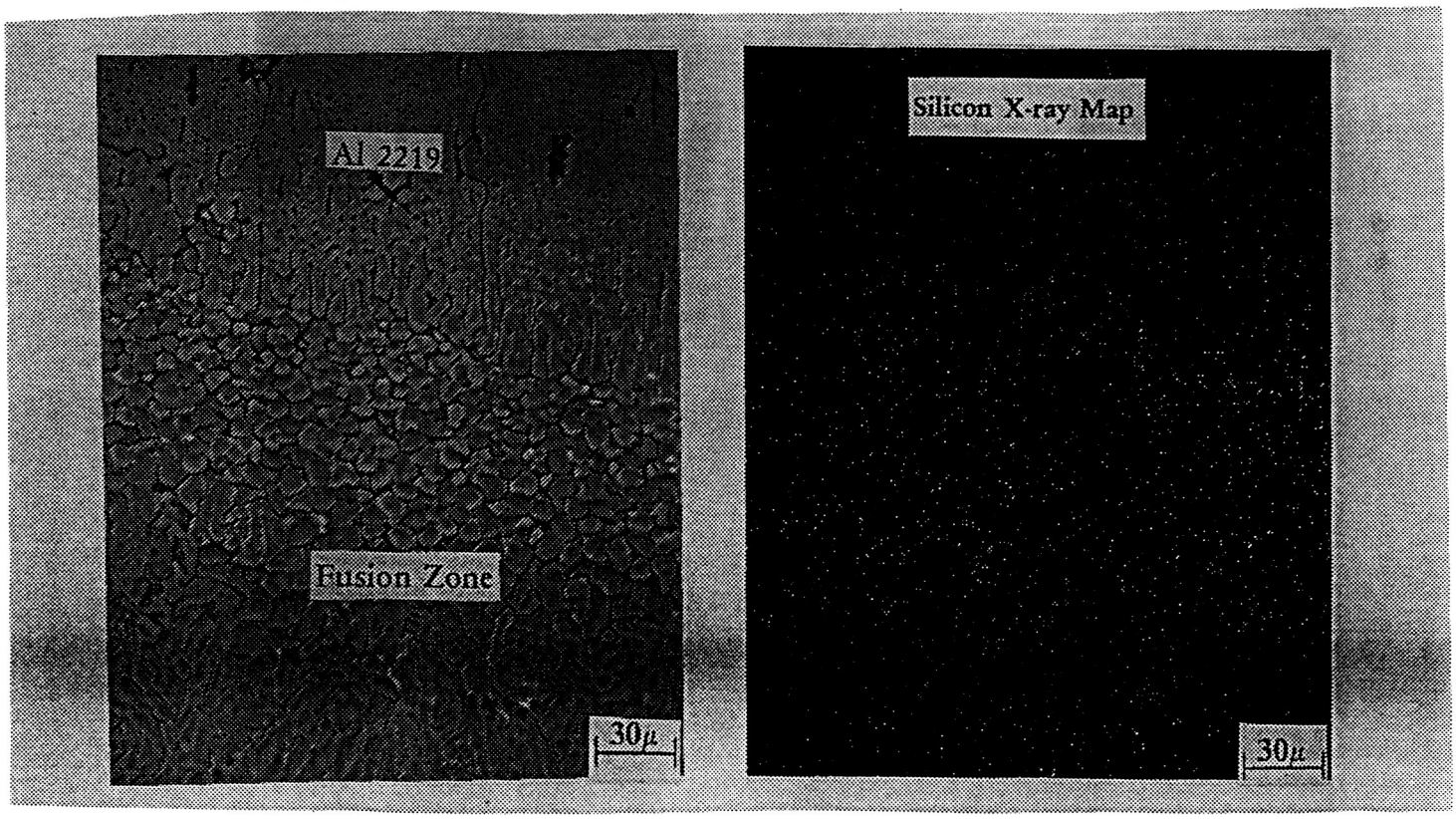

Figure 5 - Micrograph of the Al2219/weld interface (a) SEM micrograph (b) Silicon X-ray map of the interface.

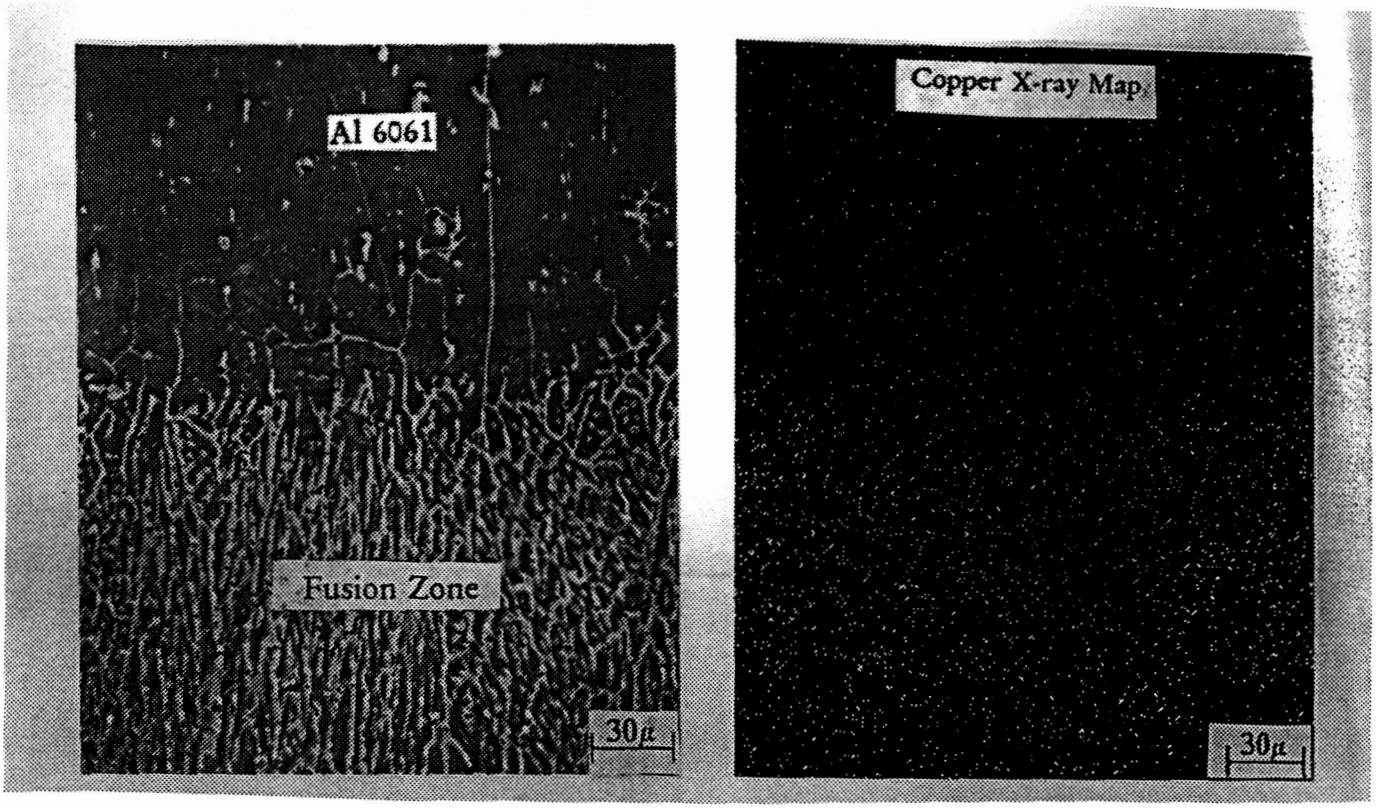

Figure 6 - Micrograph of the Al6061/weld interface (a) SEM micrograph (b) Copper X-Ray map of the interface.

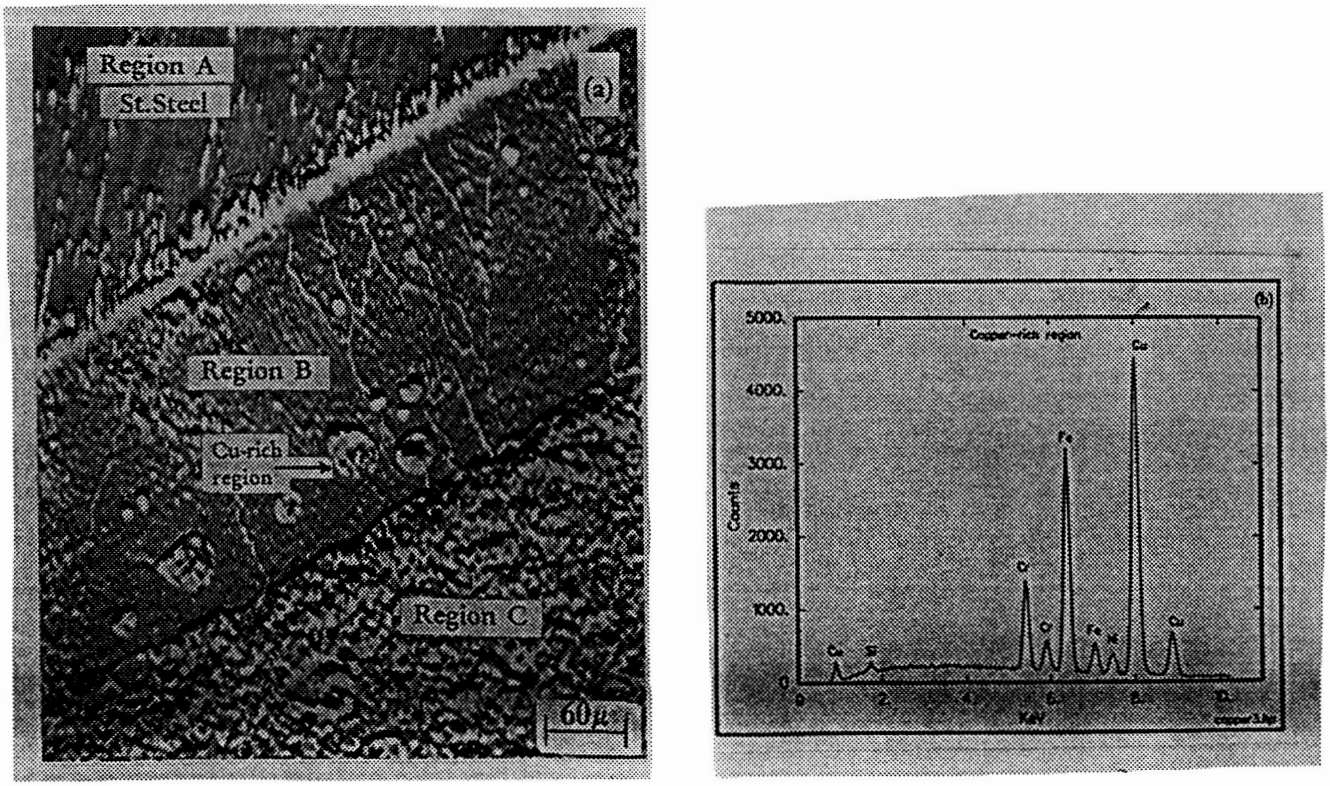

Figure 7 - SEM micrograph showing the three regions in the stainless steel/weld interface. Region A: Base steel structure, Region B: Steel fusion zone, Region C: Copper steel fusion zone. Figure 7(b): EDS spectra of copper rich region.

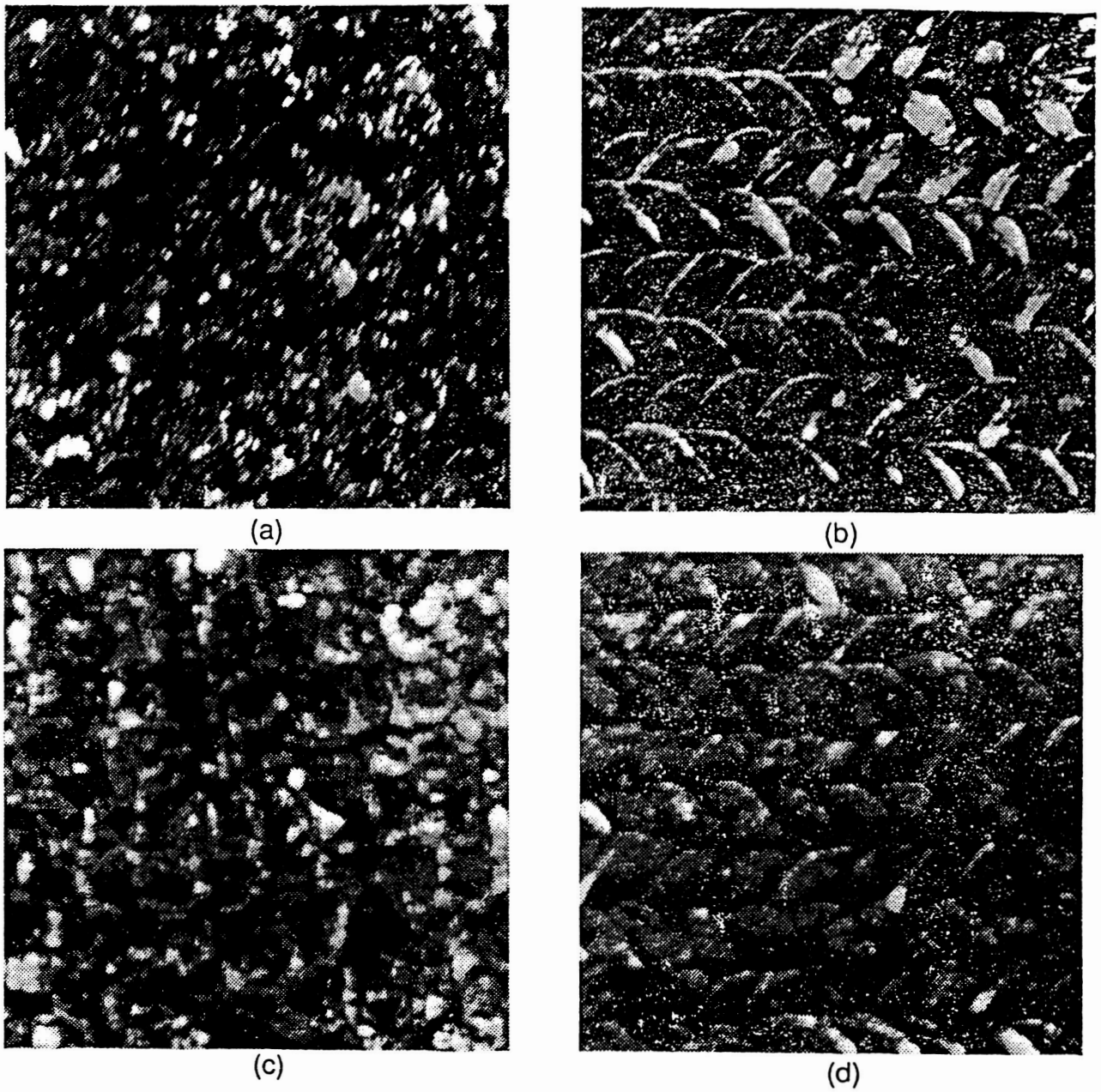

Figure 12 - Narloy Z glazed with Nd:YAG laser (a) as received surface, 0.62 Joules, (b) as-received surface, 1.90 Joules, (c) sanded surface, 0.62 Joules, and (d) sanded surface, 1.90 Joules.

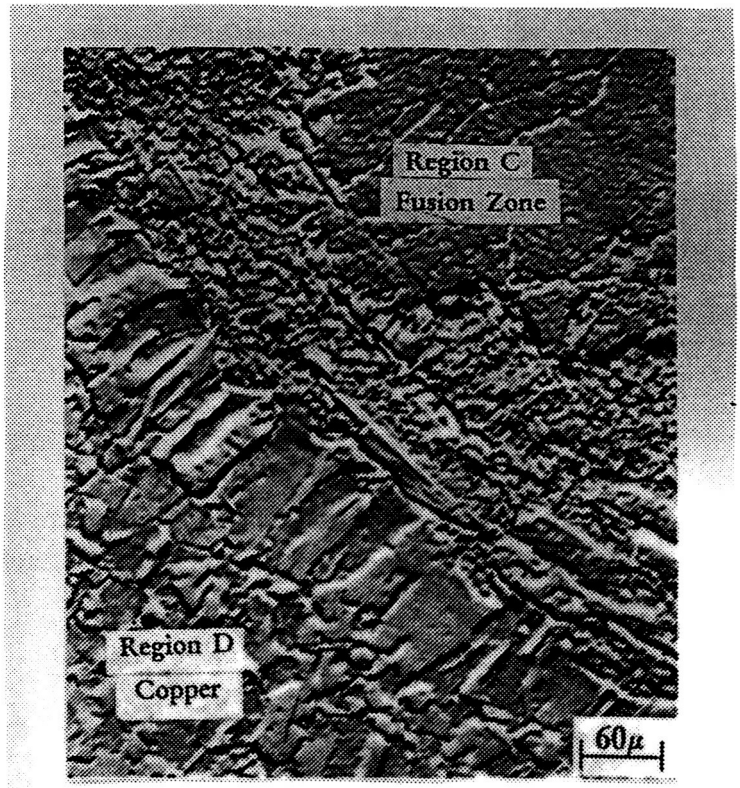

Figure 8 - SEM micrograph showing the copper-weld interface. Region C: Copper steel fusion zone, Region D: Copper heat affected zone.

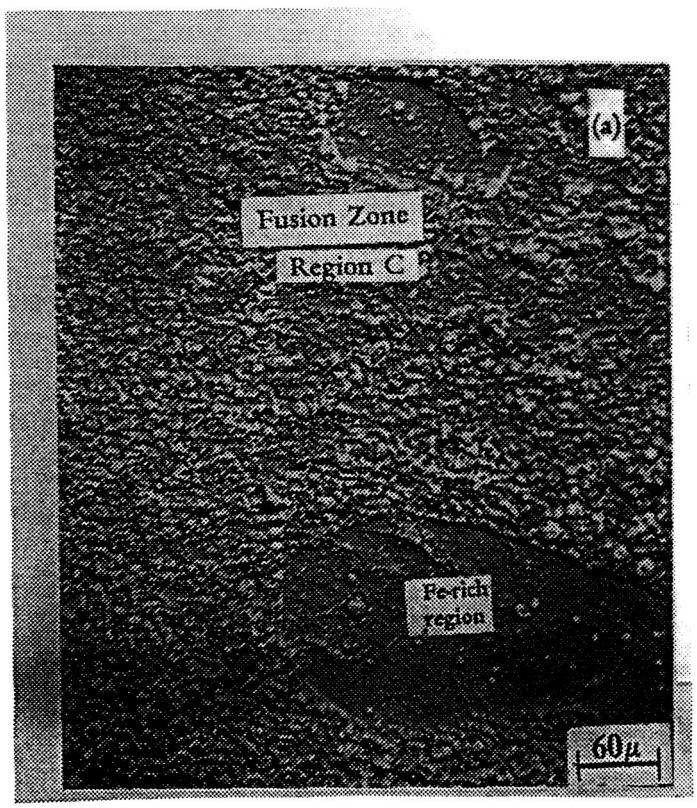

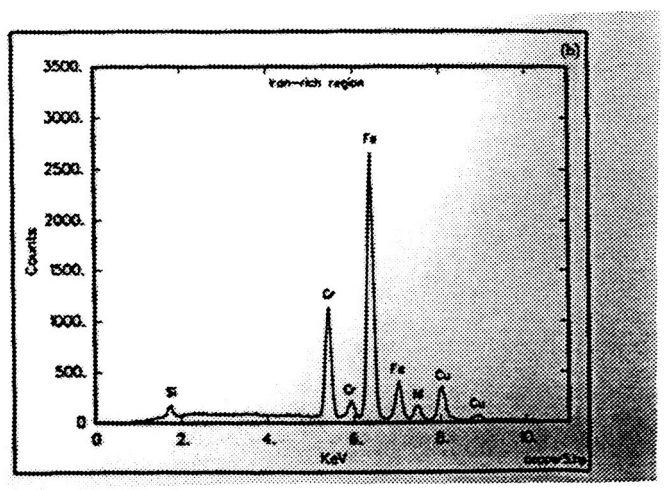

Figure 9(a) SEM micrograph showing the copper-steel fusion zone. Figure 9(b): EDS spectrum of the iron rich regions in Region C.

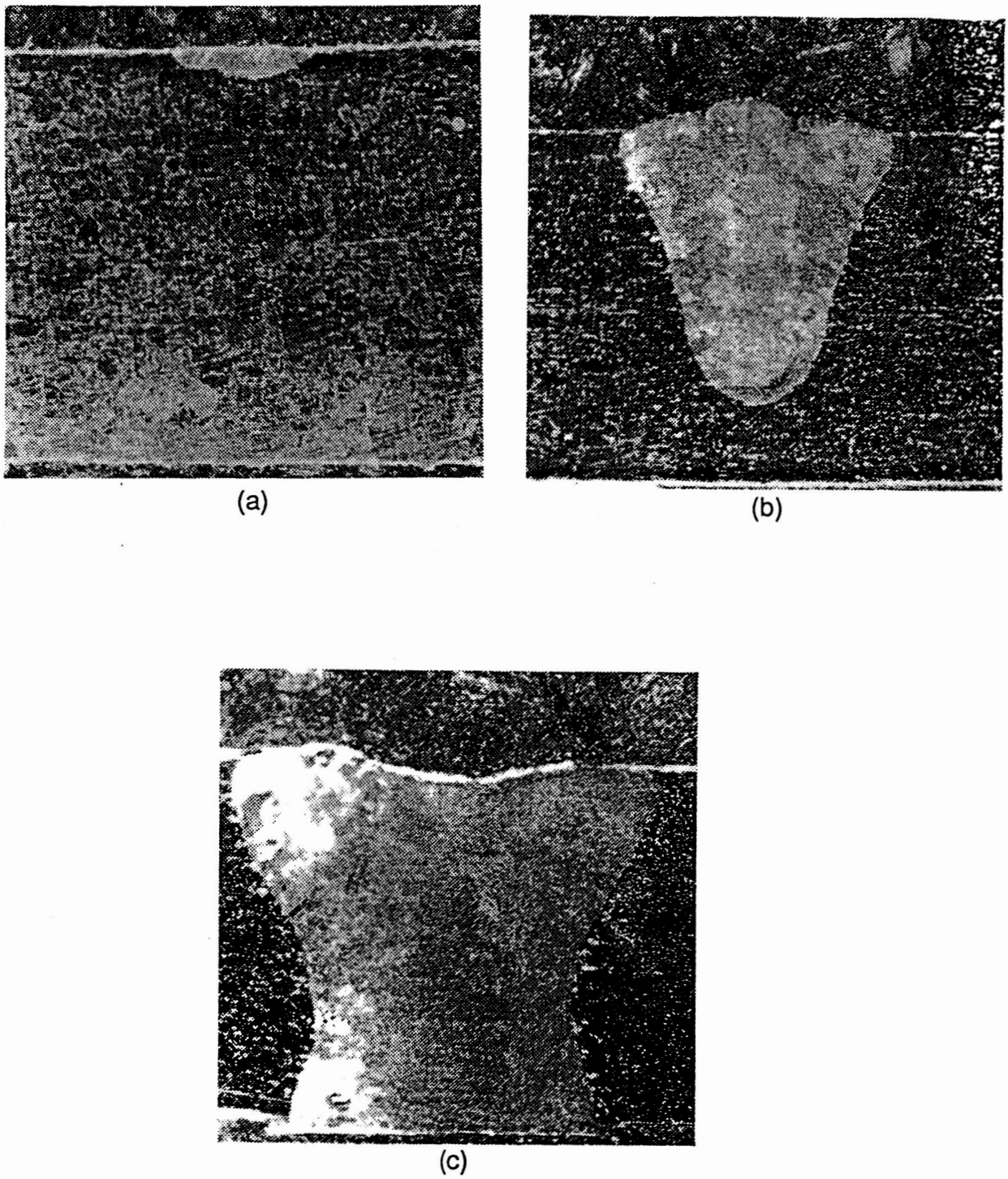

Figure 10 - Glazed Narloy Z Cross-Sections (a) Oxidized Surface, -4 Focus, 25mm/sec, (b) Graphite Paste on Surface, +1 Focus, 25mm/sec, and (3) As-Received Surface, +1 Focus, 12.5mm/sec.

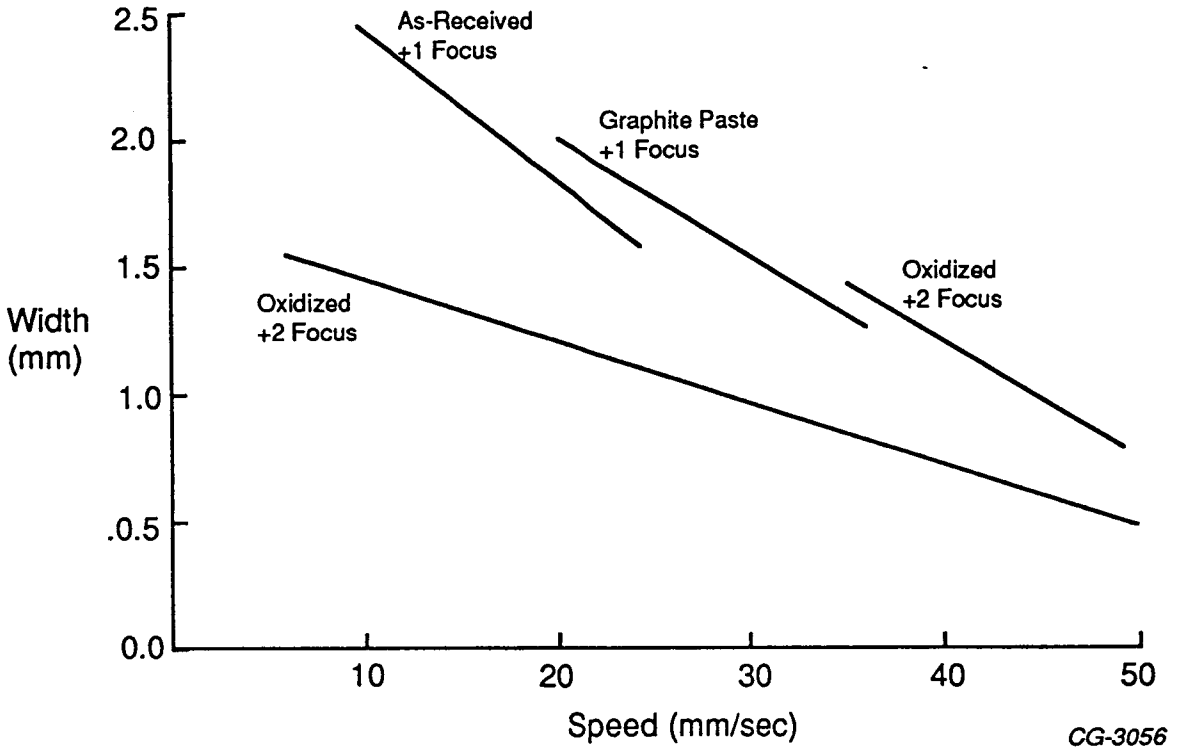

Glaze Track Widths as a Function of Processing Speed for Different Surfaces and Focal Locations.

Figure 11 - Glaze track widths as a function of processing speed for different surfaces and focal locations.